Environmental Science Processes & Impacts

ROYAL SOCIETY OF CHEMISTRY

PAPER

View Article Online
View Journal | View Issue

Cite this: *Environ. Sci.: Processes Impacts*, 2026, **28**, 793

Speciation and partitioning: a survey study of rare earth elements (REEs) in coal fly ash

Estefania Garcia, Yinghao Wen, Pan Liu and Yuanzhi Tang *

Received 22nd October 2025
Accepted 29th January 2026

DOI: 10.1039/d5em00857c

rsc.li/espi

Rare earth elements (REEs) are crucial for technological advancement in semiconductors, artificial intelligence development, and defense technologies. With the growing demand for and heavy import reliance of the U.S. on REEs, identifying and developing sustainable domestic REE feedstocks such as coal fly ashes (CFAs) is critical. In this study, the chemical speciation of yttrium (Y) as an REE probe was characterized at the bulk- and micro-scales in CFAs using synchrotron X-ray absorption spectroscopy (XAS). The results from bulk X-ray absorption near edge structure (XANES) showed bulk speciation primarily as a Y oxide, followed by Y incorporation into phosphate, iron oxide, and/or glass phases. Micro-X-ray fluorescence microscopy (μ-XRF) and μ-XANES showed varied Y speciation and co-localization with other REEs within the same particle, consistent with the heterogeneous nature of CFA particles. Sequential chemical extraction indicated that REEs were mainly present in the residual fraction typically associated with glass, aluminosilicate, or iron oxide phases. The second highest fraction of REEs was found in the reducible fraction associated with carbonates and partially dissolved iron oxide phases. However, the fractions of certain REE species may have been over- or underestimated due to the intrinsic limitations of XAS analyses. Therefore, a complementary suite of analytical or characterization techniques is needed to fully understand the REE speciation in complex matrices such as CFA and evaluate the related extractability for resource extraction and recovery purposes.

Environmental significance

Coal fly ashes (CFAs), a byproduct of coal combustion, contain significant concentrations of rare earth elements (REEs) that are essential for clean energy and defense technologies. Understanding the chemical speciation and partitioning of REEs in CFAs is critical for evaluating their environmental mobility and recovery potential as an alternative REE source. This study provides a systematic, multi-scale characterization of REE speciation across CFAs from major U.S. coal basins using synchrotron-based X-ray absorption and fluorescence spectroscopy. Results reveal that REEs predominantly occur as oxides, phosphates, and glass-associated phases with strong spatial heterogeneity. Such speciation governs both environmental stability and extractability during potential resource recovery. The findings inform about strategies for sustainable REE extraction from coal combustion residues while mitigating environmental risks associated with their disposal and reuse.

1. Introduction

Rare earth elements (REEs) are critical for technologies in clean energy (*e.g.*, wind turbines, electric vehicles, *etc.*), energy storage, electronics (*e.g.*, smartphones, electronic displays, *etc.*), and defense (unmanned aerial vehicles, submarines, *etc.*) applications.[1,2] REEs are composed of the lanthanide series as well as scandium (Sc) and yttrium (Y), due to their similar physical and chemical properties.[1] REEs are typically divided into light REEs (LREEs; La to Gd) and heavy REEs (HREEs; Y, Tb to Lu).[3] Despite the similar concentration of REEs in Earth's crust compared to other transition metals such as Zn and Cu, REEs typically do not occur as concentrated and readily exploitable ore deposits. Instead, REEs are commonly dispersed as trace phases in minerals such as phosphates (*e.g.*, monazite, apatite, and xenotime), carbonates (*e.g.*, bastnäsite and limoriite), silicates (zircon and allanite), as well as other adsorbed phases such as ion-adsorption clays.[4–6] As a result, REEs are often acquired as byproducts from the mining of other resources including iron (*i.e.*, Bayan Obo) and phosphate.[7,8] There are several pitfalls with traditional REE mining, including negative environmental impacts[9] and high operating and capital costs.[10] Due to the rapid advancement of modern technologies across various sectors, the demand for REEs has been steadily rising over the past few decades. More importantly, the current geopolitical environment has highlighted the heavy import reliance of REEs and the lack of sizeable domestic operational REE processing facilities in the U.S.[11] Therefore, identifying non-conventional and alternative REE resources and developing viable technologies for REE recovery are critically needed.

School of Earth and Atmospheric Sciences, Georgia Institute of Technology, 311 Ferst Drive, Atlanta, Georgia 30332, USA. E-mail: yuanzhi.tang@eas.gatech.edu

Previous research has explored a variety of non-conventional or waste materials as potential REE resources, including mined kaolin,[12,13] red mud,[14,15] municipal solid waste incineration ash,[16–18] and coal fly ashes (CFAs).[19–23] Among these alternative resources, CFAs have garnered much attention due to the long-established energy infrastructure, an estimated \$8.4 billion value of REE oxides from legacy CFAs between 1972 and 2021 (based on 2020 market values),[24] and continued production. Recovering REEs from CFAs may reduce the remediation costs and environmental impacts associated with conventional REE mining and facilitate beneficial utilization of CFAs.[25] Furthermore, REE recovery from these combustion byproducts may also mitigate the environmental impacts of direct landfilling and valorize waste.[16,26] CFAs have been extensively characterized in terms of mineral phases, morphology, average particle size, and major and trace metal compositions (*e.g.*, hazardous trace metals).[27–30] As a potential REE resource, CFAs have also been investigated for REE concentrations, REE associated phases and transformation, and extraction techniques.[22,23,26,31–34] However, systematic studies on the influence of coal source/type and combustion conditions on the molecular scale REE speciation and partitioning are still lacking. REE concentrations and their mineral association in CFAs are affected by the original coal source/type. Combustion conditions (*e.g.*, furnace type, emission control, *etc.*) further alter the chemical form and partitioning of REEs during coal combustion. In sum, these factors heavily influence the molecular-scale chemical speciation, bonding environment, and physical distribution of REEs in CFAs, which directly impact the effectiveness of recovery technologies.

The Electric Power Research Institute (EPRI) recently performed a survey study on current coal electrical generating units (EGUs) in the U.S.[35] CFAs were collected based on this survey study with detailed information on coal and combustion conditions including furnace type, particulate matter and emissions control. Initially, coal formation occurs through the decomposition of vegetation and their accumulation in swamps, forming peat. Over millions of years, erosion or flooding may increase the burial depth of this peat and lead to the formation of various coal ranks, based on burial depth and temperature.[36] These coal ranks progress as first peat, then lignite, sub-bituminous, bituminous, and lastly anthracite.[37,38] During the pulverized coal combustion process, coal combustion occurs in the furnace primarily through tangential (burners at each corner) or opposed (burners on opposite walls) furnaces. Alongside electricity generation is also flue gas generation. Before this flue gas is released into the environment, it undergoes these sequential environmental controls: nitrogen oxide (NOx), particulate matter, and sulfur oxide (SOx) removal. In the U.S., common NOx emission control strategies were found to be selective catalytic reduction (SCR) and the use of low-NOx burners, while particulate matter control, CFA being particulate matter, was found to be mainly achieved with baghouse filters (BHs) or electrostatic precipitators (ESPs). Lastly, SOx control approaches primarily included wet-flue gas desulfurization (WFGD) or the use of low-sulfur coal.[35] The bulk composition, mineralogy and surface characteristics of CFAs were characterized by X-ray fluorescence spectroscopy (XRF), inductively coupled plasma mass spectrometry (ICP-MS), X-ray diffraction (XRD), and surface area analysis. Synchrotron X-ray absorption near-edge structure (XANES) spectra of Y K-edge were collected as an REE representative to determine REE speciation, owing to its distinct absorption edge, minimal interference, and relatively high abundance. Y speciation at the micron-scale was investigated using micro-X-ray fluorescence microscopy (μ-XRF) coupled with micro-XANES (μ-XANES). Investigating the influence of coal combustion conditions on REE speciation may help understand potential underlying patterns of their occurrence in CFAs and contribute to the design of extraction techniques and reduction of associated costs.

2. Materials and methods

2.1 Sample collection

CFAs were obtained by the EPRI from 6 coal-fired electrical generating units (EGUs), based on representative conditions for EGUs from across the U.S.[35] Representative coal basins include the Powder River Basin (PRB), Illinois Basin (ILB), and Northern Appalachia (N. App), where N. App is classified as Pennsylvania and certain counties of New York, Maryland, and Ohio.[39] Table 1 details these representative parameters as well as coal type (sub-bituminous or bituminous), furnace type (tangential or opposed), NOx emission control method (selective catalytic reduction, SCR, or low NOx burners), and fly ash capture method (electrostatic precipitator, ESP, or baghouse filter, BH).

2.2 Bulk characterization

Samples were characterized for mineral phases, average particle size, bulk density, surface area, volatile content (Loss on Ignition, LOI), major elemental composition, and REE concentrations. Mineral phases were identified using XRD on a Malvern PANalytical Empyrean X-ray diffractometer. Data collection was conducted at 45 kV, 40 mA, a step size of 0.01° in 2θ, and $2\theta = 10$ to 70°, with spectra normalized by quartz (101), shown in Fig. S1.[40] The particle size, surface area, and density were analyzed by SGS TEC Services using ASTM C188-17 and laser diffraction. The LOI, elemental composition, and REE concentrations were analyzed by the Peter Hooper GeoAnalytical Lab at Washington State University. The major elemental composition was performed with a Thermo Scientific ARL X-ray fluorescence spectrometer. REE concentrations were determined by total digestion using a perchloric fume hood, and solutions were analyzed with an Agilent 7700 ICP-MS equipped with a collision cell.[40]

2.3 Synchrotron microscopy and spectroscopy analyses

2.3.1 Y K-edge bulk XANES. Bulk Y K-edge XANES spectra were collected for CFAs and model compounds at Beamline 11-2 at Stanford Synchrotron Radiation Lightsource (SSRL, Menlo Park, CA) and Beamline 5-BM-D at the Advanced Photon Source (APS, Lemont, IL, USA). Samples 9, 10, 11, 12, 13, 14, 1B, and 2S were selected for bulk XANES analysis based on representative

Table 1 CFA sample information and combustion parameters[a][40]

Sample ID	Coal source	Coal type	Furnace type	SOx control	NOx control	Particulate matter control
1	PRB	Sub.	Opposed			ESPc
2	PRB	Sub.	Opposed			ESPc
3	PRB	Sub.	Opposed			ESPc
4	PRB	Sub.	Opposed			ESPc
5	PRB	Sub.	Opposed			ESPc
6	PRB	Sub.	Opposed			ESPc
7	PRB	Sub.	Opposed			ESPc
8	PRB	Sub.	Opposed			ESPc
9	PRB + MSW	85% sub. + 15% bit.	Tangent			ESPc
10	ILB	Bit.	Tangent	WFGD		ESPc + BH
11	ILB	Bit.	Opposed	WFGD		ESPc + BH
12	ILB	Bit.	Opposed	WFGD		ESPc + BH
13	N. App.	Bit.	Opposed		SCR	ESP
14	N. App.	Bit.	Opposed		SCR	ESP
1B	ILB	Bit.	Tangent	WFGD	SCR	ESPc/BH
2S	PRB	Sub.	Tangent	WFGD	SCR	BH

[a] PRB: powder river basin, MSW: municipal solid waste, ILB: Illinois basin, N. App.: North Appalachia, Sub.: subbituminous, Bit.: bituminous, WFGD: wet flue gas desulfurization, SCR: selective catalytic reduction, ESP(c): electrostatic precipitator (cold side), and BH: baghouse.

coal parameters in Table 1. Samples and model compounds were finely ground with an agate mortar and pestle and mounted in a sample holder. Energy calibration used $Y_2(CO_3)_3\cdot 2–3H_2O$ (tengerite, Y K-edge at 17 056.5 eV). 4–5 scans were collected for each sample and 2–5 scans for model compounds in fluorescence and transmission modes, respectively. Spectra were processed using the software Athena for energy calibration and linear combination fitting (LCF) analysis.[41] LCF was performed in the energy range from −50 to +150 eV, and fits were chosen based on individual component weight percentages ≥10% and based on criteria listed in Liu *et al.*[31] Fits with the smallest *R*-factor were chosen, and a third component was added if the *R*-factor decreased by ≥10%.

2.3.2 μ-XRF and μ-XANES. Petrographic thin sections of CFAs were prepared by the National Petrographic Service on quartz slides. Samples selected for μ-XRF and μ-XANES analyses were 5, 8, 9, 10, 11, 12, 13, 14 1B, and 2S, since samples 1–8 had similar coal parameters (Table 1). These thin sections were analyzed by synchrotron μ-XRF and μ-XANES at Beamline 2-3 at SSRL and Beamline 13-ID-E at APS. μ-XRF analysis involved collecting large area maps with a step size of 10 μm and a dwell time of 50 or 100 ms at 17.2 keV. Once Y hot spots were located, smaller maps were collected at a step size of 1 or 2 μm and a dwell time of 25 or 50 ms at 17.2 keV. μ-XANES spectra were processed with SixPack and Athena, whereas μ-XRF were processed with SMAK.[42,43] Energy calibration used $Y_2(CO_3)_3\cdot 2–3H_2O$ (tengerite K-edge at 17 056.5 eV) or yttrium foil (K-edge at 17 038 eV), and 3–4 scans were collected per sample. LCF results were selected based on the same parameters for bulk XANES.

2.4 Statistics

To assess the significance of coal combustion parameters on REE speciation or REE concentrations, non-parametric tests for quantitative data were applied. The Mann–Whitney *U* test (Wilcoxon test) and Kruskal–Wallis test were performed in RStudio using "wilcox.test()" and "kruskal.test()".[44] A 95% confidence level interval was used for both tests, so a *p*-value <0.05 is statistically significant.

2.5 Sequential extraction

Sequential chemical extraction was performed to target REE fractions following previous procedures.[31,45] Initially, 0.5 g of coal fly ash was reacted with 8 mL of 1 M $MgCl_2$ (pH 7) at room temperature for 1 hour at 140 rpm to target fraction 1 (ion-exchangeable). Next, 16 mL of 1 M NaOAc (pH 5) was added, and the mixture was shaken at 140 rpm for 6 hours (fraction 2, associated with carbonates). Then, the residue was reacted with 20 mL of 0.04 M NH_2OH HCl in 25% (v/v) CH_3COOH at 96 °C for 6 hours with agitation every 30 minutes (fraction 3, Fe–Mn oxides). Lastly (fraction 4, oxidizable phase), 3 mL of 0.02 M HNO_3 and 5 mL of H_2O_2 (30%) were added to the residue, the pH was adjusted to 2 and heated at 85 °C for 3 hours (repeated). After the mixture was cooled, 5 mL of 3.2 M CH_3COONH_4 in 20% (v/v) HNO_3 was added. After each reaction step, the mixture was centrifuged at 10 000 rpm for 10 minutes, the supernatant was syringe filtered (0.22 μm) and acidified for ICP-MS analysis, and the residue was rinsed with deionized water and re-centrifuged. The REEs associated with the residue were calculated based on REE concentrations leached from each step and the total REE concentration, determined by total digestion.

3. Results and discussion

3.1 Bulk composition

Bulk CFA properties are presented in Table S1, including the average particle size, bulk density, and ASTM-C618. Overall, 8 samples are potential candidates for class C based on calcium oxide wt% ((CaO) ≥18%), 7 samples are class F (≤18% CaO), and one sample does not meet either composition requirements (sample 10). XRD analysis identified periclase, portlandite, mullite, magnetite, hematite, calcite, anhydrite, thenardite, lime, gehlenite, and quartz as the major mineral phases, which agreed with previous studies (Fig. S1).[46,47]

3.1.1 REE concentrations. The U.S. Department of Energy (DOE) has designated a total REE concentration of 300 ppm as commercially viable for recovery from coal and coal by-products.[48] Table S2 summarizes the REE concentrations of CFAs in this study. Samples that contain over 300 ppm of total REEs include samples 5, 6, 8, 9, and 2S from the Powder River Basin, samples 11, 12 and 1B from the Illinois Basin, and samples 13 and 14 from Northern Appalachia. To better understand the trends in REE enrichment or depletion for this sample set, REE concentrations were normalized to the upper continental crust (Fig. 1A).[49] An M-type distribution that is typical for CFAs, with $\mathrm{Gd_N/Lu_N} > 1$ and $\mathrm{La_N/Sm_N} < 1$,[31,50,51] can be observed in Fig. 1A, where samples are presented by coal basin source (blue (PRB), green (ILB), and yellow (N. App.)). Based on Fig. 1A and previous work,[40] sample 10 is quite different compared to other CFAs. To delve into REE composition based on coal basin for CFAs, averages for the normalized values were calculated. Based on Fig. 1B, CFAs from N. App have a higher $\mathrm{Gd_N/Lu_N}$ ratio, suggesting a higher enrichment of MREEs compared to ILB and PRB. However, the averages of PRB and ILB show a slight enrichment in HREEs ($\mathrm{La_N/Lu_N} < 1$) with values of 0.77 and 0.75 compared to N. App. samples (0.96). This differs from a previous study where CFAs from the Appalachian (APP) basin showed greater HREE and MREE enrichment compared to the PRB and ILB.[52] Ce anomalies (Ce*) are not apparent in Fig. 1A, and based on values of 0.9–1 ($\mathrm{Ce^* = 2Ce/(La + Pr)}$),[31] the same was true for Eu anomalies (Eu*), which were all 1 ($\mathrm{Eu^* = 2Eu/(Sm + Gd)}$).

Based on previous work,[50] REE outlook coefficients (C_{out}) were calculated as follows:

$$C_{\mathrm{out}} = \left(\frac{\mathrm{Nd + Eu + Tb + Dy + Er + Y}}{\sum \mathrm{REY}}\right) \Big/ \left(\frac{\mathrm{Ce + Ho + Tm + Yb + Lu}}{\sum \mathrm{REY}}\right).$$

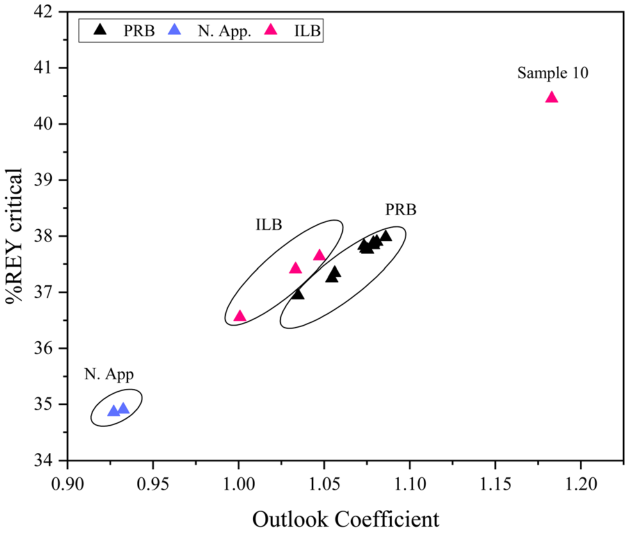

Fig. 2 Outlook coefficient and critical REY% for CFAs calculations based on Seredin and Dai,[50] samples are naturally grouped by coal basin.

The REE outlook coefficient takes into consideration the amount of critical REEs (*i.e.*, Nd, Eu, Tb, Dy, Y, and Er), and a higher outlook coefficient indicates a more promising REE source. The results for REE outlook coefficients are plotted against critical REY% in Fig. 2, and CFAs fall into 3 groups based on coal basin. In Fig. 2, CFAs from the N. App basin are shown in blue with a C_{out} of 0.93 and a critical REY% of 35%, indicating a less promising source of REEs compared to CFAs from PRB (C_{out} of 1.03–1.09 and critical REY% of 37–38%). Sample 10 is not grouped with the remaining ILB samples, suggesting it as an outlier and a more promising REE source than the remaining CFAs. Specifically, sample 10 has a C_{out} of 1.18 and a critical REY% of 40%, the highest in this sample set. In terms of bulk properties, sample 10 has the lowest particle size (8.3 μm), $\mathrm{SiO_2}$ content (24.13%), and $\mathrm{Al_2O_3}$ (11.24%)

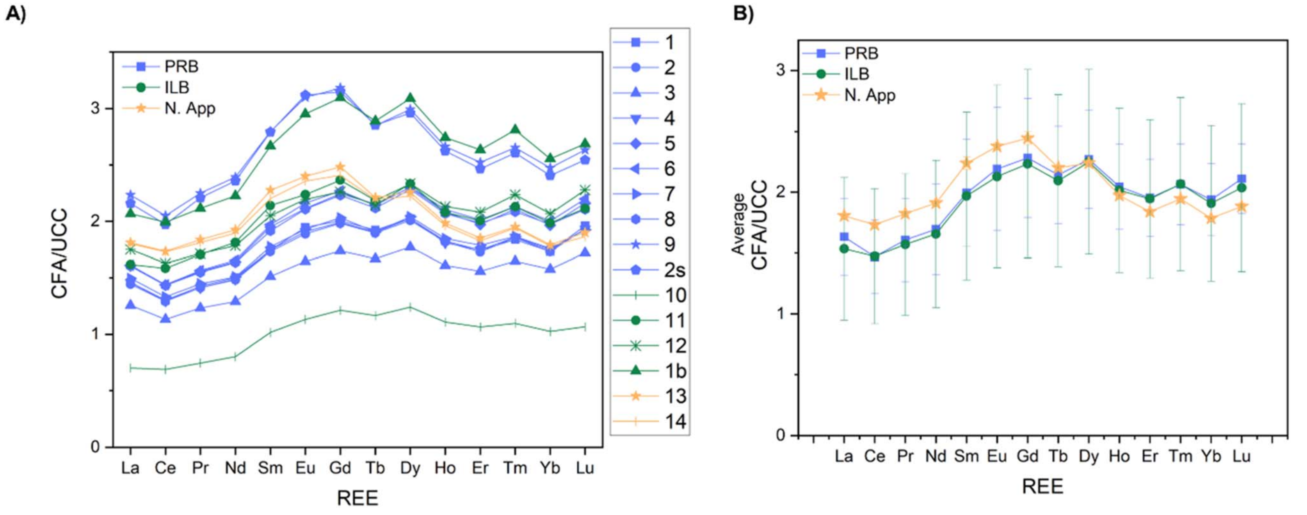

Fig. 1 (A) REE concentrations (excluding Sc and Y) in the CFA samples normalized to the upper continental crust (UCC) for each sample; (B) average concentration for all samples from PRB, ILB, and N. APP basins.

content, concurrently with the largest LOI (9.72). Moreover, sample 10 fails to meet standard specifications in ASTM C618-22, so it is neither class C nor class F fly ash. Generally, CFAs that fail to meet these standards are disposed of. Overall, all CFAs in this study fall within cluster II (C_{out} of 0.7–1.9 and critical REE of 30–51%) according to Seredin and Dai's study and are promising sources of REEs.[50]

3.2 Bulk Y speciation by bulk XANES

While characterizing the mineralogy, morphology, and REE concentrations in CFAs may offer valuable insight into potential REE recovery, synchrotron XAS analyses allow us to determine the primary chemical speciation of REEs and acquire a deeper understanding of REE extractability. Bulk Y K-edge XANES spectra were analyzed to determine its bulk speciation using a library of model compounds. Model compounds for Y were consistent with previous work in CFAs[31–33] and are grouped as dissolved REEs and REE-bearing carbonates, oxides, organics, iron oxides, phosphates, glass phase, and zircon (Fig. S2). Details on model compounds are listed in Table S3.[31] Relative percentages of model compounds were identified in CFAs using linear combination fitting to predict Y speciation (Table 2). XAS spectra of samples 9, 10, 11, 12, 1B, and 2S are illustrated in Fig. 3A. The LCF results reveal that all 8 samples contain 28–78% of Y_2O_3, and the majority of samples (12, 13, 14, 1B, and 2S) contain 29–41% of Y-phosphate (Fig. 3B). Samples 10 and 12 are predicted to have 22–26% of Y associated with iron oxide, and sample 9 has 72% of Y in the glass phase, as shown in Fig. 3B.

Although pure REE oxides are not commonly found in coal,[50] they can exist as trace phases in silicates (substitution into zircon), phosphate minerals (*e.g.*, monazite, xenotime, and apatite), carbonates (*e.g.*, bastnäsite), iron oxides, and organic matter.[21,50,53,54] Overall, bulk XANES results reveal Y oxide (Y_2O_3) as a major Y species in CFAs (28–78%), as REE carbonates and organics will decompose into REE oxides at temperatures greater than 300 °C.[22,55,56] However, organics may be found in CFAs due to their incomplete combustion, leading to the formation of polycyclic aromatic hydrocarbons (PAHs).[57] While Taggart *et al.* identified REE-doped glass (22–76%) in all CFAs, in this study, only 1 sample was found to contain a significant glass fraction (72%).[32] The results from bulk XANES were similar to previous studies where CFAs comprised 18–55% of REE oxides, 20–30% of phosphates, and 20–35% of iron oxides, respectively.[31,32] The representativeness of results from these previous studies were limited by their smaller sample sizes. One study included 4 CFAs (two from NIST and two from the southeastern U.S.), while another study had 9 samples from the Appalachian, Powder River, and Illinois basins, along with a sample from South Africa. Acknowledging the limitations from previous studies provides a context for limitations in this study, which include using Y as a proxy for all REEs and sample size. Using Y as an REE proxy may highlight the behavior of heavy REEs compared to light REEs; however, in the next section, μ-XRF images show the colocalization of other REEs with Y. An additional factor to consider is the sample size of this study. There are 16 representative samples, but only 8 were analyzed. Although more data would have been provided if all samples were analyzed, the results may have been repetitive compared to our previous arsenic and selenium studies.[40,58] Future work may involve acquiring more samples under representative combustion conditions.

3.3 Micro-scale Y speciation by μ-XANES

Bulk XANES spectra indicated that REEs in CFAs are primarily present as REE oxides, with the remaining fractions of REEs associated with phosphates, iron oxide, or glass. Complementary to the global view of REE speciation by bulk XANES is the micron scale analysis of REE speciation within individual particles using μ-XANES. Elemental distribution maps obtained by μ-XRF were used to identify the elemental association of Y and locate Y-bearing particles (hot spots), which were subsequently analyzed by μ-XANES for micro-scale Y speciation. Based on CFA parameters (*e.g.*, combustion conditions and coal source), 10 out of the 16 samples were selected for μ-XANES. Among the Y-bearing particles located for the 10 samples, some spectra were too noisy to be analyzed by LCF, possibly due to the low Y concentration. A complete list of LCF results for μ-XANES are shown in Table S4.

According to μ-XRF images, the average size of Y-bearing particles ranged from ~8 to ~90 μm, consistent with the typical size range reported by previous studies using different techniques (*e.g.*, 10–20 μm by μ-XRF; 4–35 μm and 1–20 μm by electron microscopy).[32,33,59] Among the 44 fitted μ-XANES spectra, 39 contained Y_2O_3 at 36–99%. Similarly, among the 44 hot spots with fitted μ-XANES spectra, 6 of them were predicted

Table 2 Linear combination fitting results of Y K-edge bulk XANES

	Y speciation%					
Sample	Y_2O_3	Glass	Hematite	Churchite ($YPO_4 \cdot H_2O$)	Sum	*R*-Factor
9	28.8 ± 3.6	72.4 ± 3.5			101.2	0.002567
10	74.7 ± 1.6		21.1 ± 1.5		95.8	0.002345
11	71.5 ± 1.3		25.6 ± 1.3		97.1	0.001615
12	68.4 ± 1.5			28.1 ± 1.5	96.5	0.001894
13	57.5 ± 1.4			39.7 ± 1.3	97.2	0.001515
14	65.5 ± 1.7			31.1 ± 1.7	96.6	0.002361
2S	70.8 ± 2.0			23.7 ± 1.9	94.5	0.003382
1B	68.8 ± 1.6			27.5 ± 1.6	96.3	0.002145

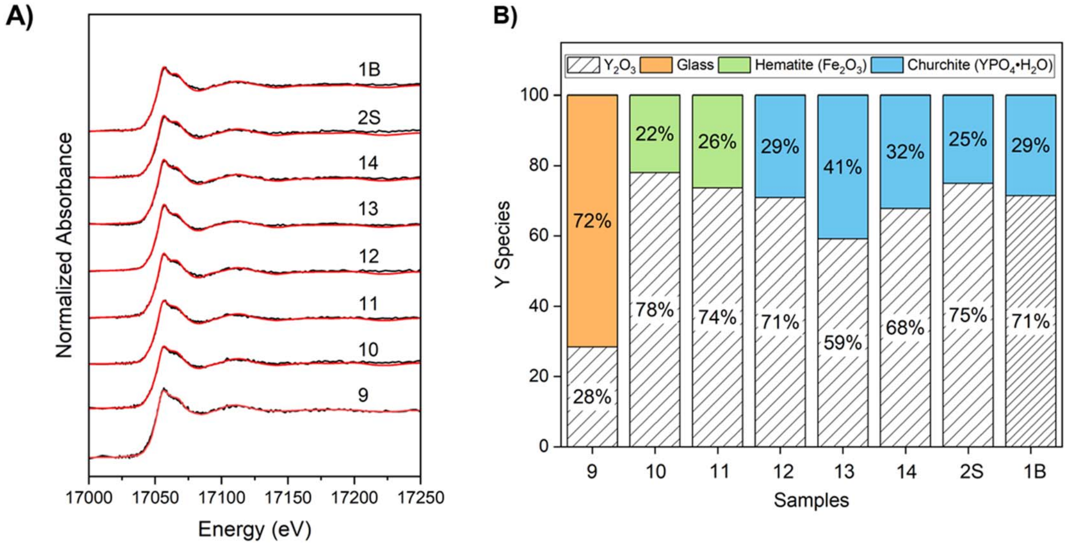

Fig. 3 (A) Y K-edge bulk XANES spectra of CFAs (black lines) and LCF results (red lines). (B) Y species determined by LCF of CFAs, summed to 100.

to contain 14–100% of Y associated with the glass phase. Both Y_2O_3 and Y-doped glass cases are discussed below.

Two hot spots (2S_11 and 2S_12) were selected from a Y-containing particle (approximately 70 μm wide) in the μ-XRF image of sample 2S (Fig. 4A). The elemental heat maps indicated that Y is co-localized with other REEs including Yb and Sm but not with Fe. The corresponding μ-XANES LCF results for 2S_11 and 2S_12 show speciation differences within the same particle: Y in 2S_11 consists of 36% Y_2O_3 and 62% zircon, while 2S_12 contains 37% Y_2O_3, 18% Y-carbonate (tengerite), and 43% zircon (Fig. 4B). The predicted Y speciation of these hot spots is notably different from the bulk XANES LCF results of sample 2S (75% Y_2O_3 and 25% Y-phosphate).

LCF results suggest that one spot within sample 14 and one within sample 1B contained Y-doped glass, with hot spots 14_02 and 1B_03 at 14% and 90% (Table S4). However, LCF results of bulk XANES for samples 14 and 1B suggest that Y is primarily present as 70% Y_2O_3 and 30% Y-phosphate (churchite). The discrepancies in the predicted Y speciation for bulk- and μ-XANES highlight the heterogeneity of REEs in CFAs, which can be ascribed to the complexity of REE host phases in coals, spatial variations in local bonding environments during combustion processes, and sampling bias of μ-XRF/μ-XANES analyses.

Moving forward, Fig. 5 features hot spots with element heat maps of Y, Ce, Si, P, Ca, and Fe in samples 1B, 8, 9, and 14. The μ-XRF images show variation in the particle size, in which smaller Y-bearing particles (≤40 μm) were observed for hot spots 8_02, 9_05, 9_04, and 14_05, while hot spots 1B_01 and 8_01 have a larger particle size (≥40 μm), with Y concentrated at

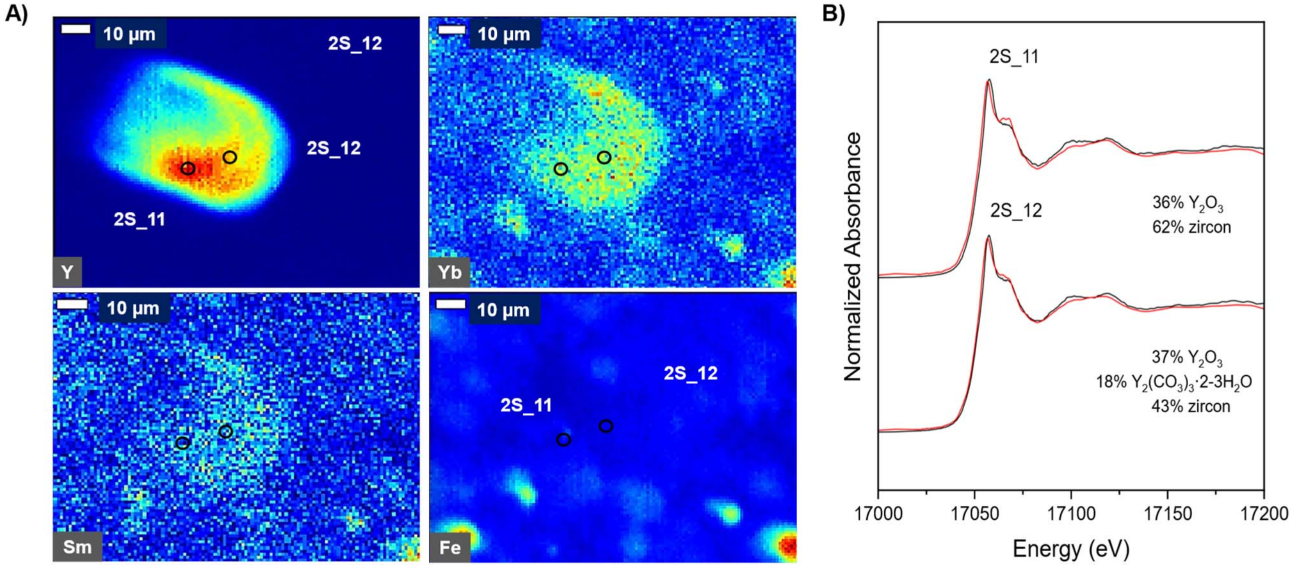

Fig. 4 (A) Synchrotron μ-XRF elemental maps for two Y-containing hot spots (shown as black or white circles) marker 1 and marker 2. (B) Y K-edge μ-XANES spectra (black lines) and LCF results (red lines) for the corresponding hot spots.

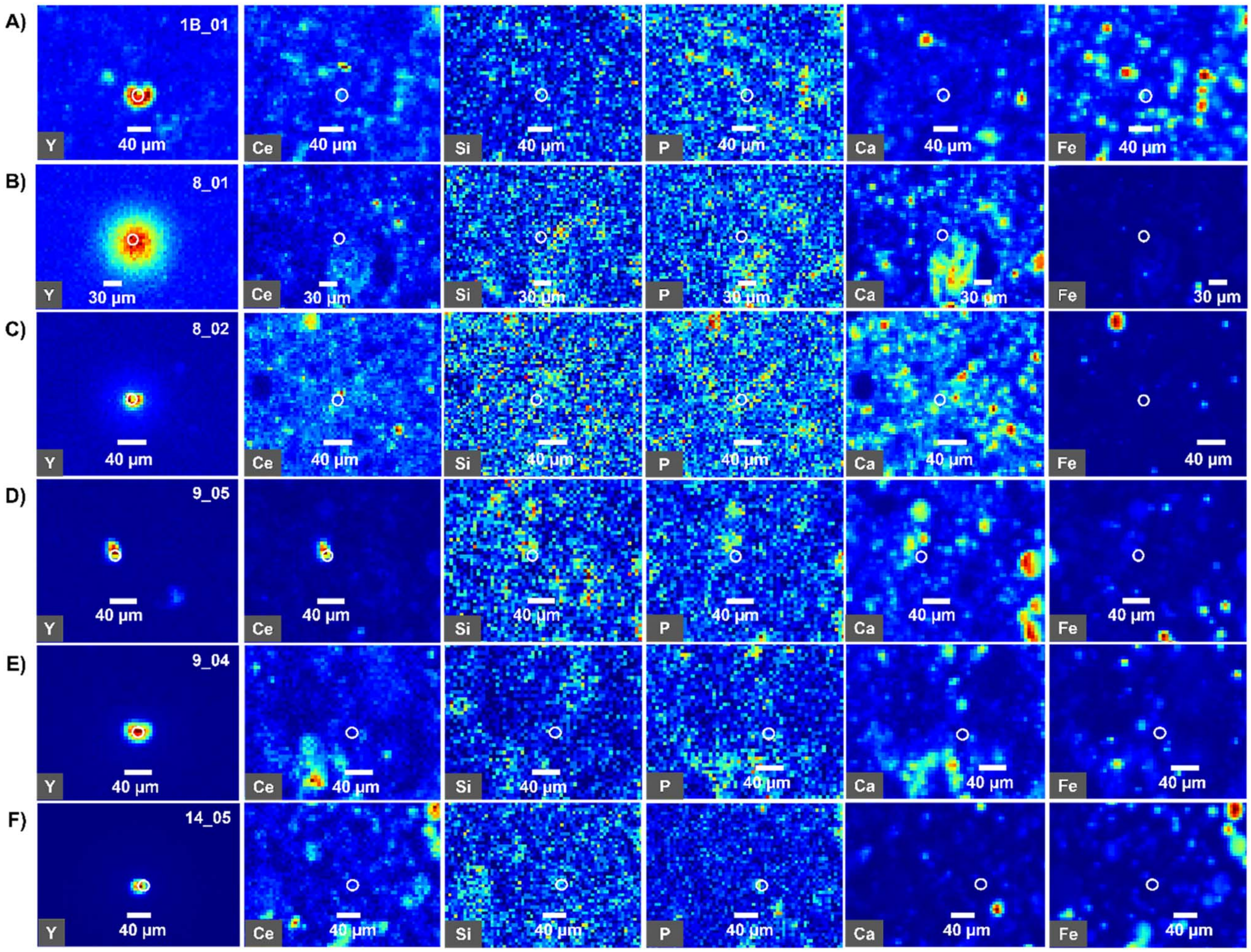

Fig. 5 Synchrotron μ-XRF maps for Y-containing hot spots (shown as black or white circles) and corresponding Ce, Si, P, Ca, and Fe elemental maps. (A) sample 1B hot spot 1B_01; (B) and (C) are sample 8 hot spots 8_01 and 8_02; (D) and (E) are sample 9 hot spots 9_05 and 9_04; (F) is sample 14 hot spot 14_05.

the curves forming a bilobed morphology (Fig. 5A). The corresponding μ-XANES spectra and LCF results are shown in Fig. S3 and Table S4. Based on the LCF results, hot spots 8_01 and 8_02 in sample 8 vary significantly in Y speciation. The hot spot 8_01 contains 59% of Y_2O_3, 29% zircon (ZrSiO4), 9% Y-phosphate (monazite), and 2.5% Y-iron oxide (hematite), and the μ-XRF maps indicate co-localization with Si (Fig. 5B). Similarly, Y in hot spot 8_02 is also co-localized with Si; however, LCF results indicated 37% zircon, 46% Y-phosphate (apatite), 11.5% Y-phosphate (xenotime), and 5.5% of Y as Y_2O_3, suggesting that this Y-bearing particle may be embedded in Si-containing phases. Additionally, LCF results for hot spot 14_05 in Fig. 5F suggest that this particle is composed of 42% Y_2O_3, 36% Y-iron oxide (hematite), 21% Y-phosphate (monazite), and 4% zircon, and the μ-XRF maps also show co-localization of Y and P. Based on LCF results, hot spots 1B_01, 9_04, and 9_05 in Fig. 5 contain 5–42% of Y as Y_2O_3, 47–93% as Y-iron oxide (hematite), and Y-phosphates (churchite, apatite, or monazite) (Table S4). μ-XRF maps for hot spot 1B_01 show co-localization with P, and the overall μ-XANES LCF results revealed sample 1B had various speciation results with either Y_2O_3, Y-glass, Y-iron oxide (hematite), Y-carbonate (tengerite), or Y-phosphate, while bulk XANES results showed Y speciation as 29% Y-phosphate (churchite) and 71% Y_2O_3. Comparably, hot spots 9_05 and 9_04 varied in Y speciation, while the overall bulk XANES revealed Y speciation as 72% Y-glass and 28% Y_2O_3.

Overall, Y_2O_3 was identified as the predominant Y-bearing phase in the 44 analyzed μ-XANES spectra, which accounts for ~31–99% of Y speciation in 35 out of the 44 fitted hot spots in the 9 CFAs (Table S4). Following that, Y-phosphates (churchite and apatite) represent ~12–69% of Y in 9 hot spots, and Y-glass accounts for ~14–100% of Y in 8 hot spots. While LCF results also suggest Y-carbonate (tengerite) as an important Y-bearing phase, it is thermally and chemically less stable than Y_2O_3, Y-phosphates, and Y-glass and thus may be formed due to incomplete coal combustion. Another possible reason is that as a mathematical tool, one limitation of LCF is that it may not be able to distinguish between the spectra of model compounds that are highly similar. The XANES spectra of Y-carbonates (including tengerite and bastnäsite) display a very similar spectral feature to that of Y-hematite, in which a strong absorption peak is observed at around 17 056 eV without any shoulder. Hence, the LCF results in this case may not reflect the actual Y speciation. Other minor mineral phases that were also associated with Y include calcite, zircon, and hematite. In addition, previous studies using μ-XANES have also reported the presence of Y as Y_2O_3, Y-phosphate, Y-carbonate, Y-iron oxide, and glass in CFAs.[31,32] Meanwhile, electron microscopy and ion microscopy have found REE particles to be associated with aluminosilicate glass, particularly glass enriched with Ca and Fe or as discrete particles.[31,34,59] In general, μ-XANES revealed varied Y speciation within the same particle and variation at a microscale compared to the overall bulk speciation results, as well as varied particle morphology with spherical and bilobed structures.

3.4 Statistical significance

Overall, characterization of REEs by XANES, with Y as a proxy, revealed the heterogeneous nature of CFAs. Since CFAs in this study are systemic, and information on their corresponding coal parameters and combustion conditions is provided, there is a need to investigate possible correlations between coal parameters, combustion conditions, REE speciation, and REE concentrations. Therefore, the influence of these quantitative coal parameter features was analyzed using the Wilcoxon rank sum test and the Kruskal–Wallis test. The Wilcoxon rank-sum test (also referred to as the Mann–Whitney *U* test) is a non-parametric statistical test that assumes data are unevenly distributed and used to test statistical significance between the two groups.[60–62] This test also produces a test statistic "W" that is used in calculating the *p*-value and may be compared to the expected W ($W_{\text{expected}} = n(n+1)/2$). The closer the W in magnitude to W_{expected} suggests no difference, while a larger magnitude suggests a potential difference, but the *p*-value is the final value that determines statistical significance.[63,64] While the Kruskal–Wallis test provides further analysis for statistical significance for >2 groups.[65,66] Properties investigated were total REE concentrations and bulk XANES K-edge linear combination fitting results: Y_2O_3, glass, hematite, and churchite% for a total of 5 properties. These properties were investigated between two groups for NOx control (SCR and no SCR), furnace type (opposed and tangential) and between three groups for coal basin (PRB, ILB, and N. APP). Although the sample size for the three different coal basins is limited to only two samples from the N. APP, this sample set contains current representative coal parameters and robust coal combustion conditions for EGUs.

The results for the Wilcoxon test are shown in Table S5 at 95% confidence interval. Table S5 shows no statistical significance between any 2 coal basins and REE concentrations (*p*-values from 0.24 to 1). However, there was a statistical significance between REE concentrations and NOx technology with a *p*-value of 0.02. This suggests that the SCR may impact REE concentrations in CFAs. Our previous work has suggested SCR impacts the oxidation state of arsenic (As) and selenium (Se) in CFAs by promoting lower oxidation states (*e.g.*, As(III) over As(V) and Se(0) and Se(IV) over Se(VI)).[40,58] There was no statistical significance between NOx technology (SCR and no SCR) and Y-bulk composition with *p*-values between 0.10 and 0.67. Lastly, there was no statistical significance between furnace type (opposed and tangential) and Y-bulk composition with *p*-values of 0.18–1. As for REE concentrations, there was no statistical significance between any two of the coal basins with *p*-values ranging from 0.24 to 1.

Meanwhile, the results for the Kruskal–Wallis test are presented in Table S6. Based on a *p*-value of 0.36, there is no statistical significance between total REE concentrations and the PRB, ILB, and N. APP coal basins (*p*-value of 0.36) or Y-bulk composition and coal basins (*p*-values between 0.11 and 0.32). The overall findings suggest that SCR may impact REE concentrations in CFAs, but future work is needed to build on these findings to examine a possible mechanism.

3.5 REE mobility through sequential extraction

As a complementary tool to bulk XANES and μ-XRF/μ-XANES, sequential extraction was used to determine the fractions associated with individual REEs, which can provide valuable information on the distribution, mobility, and chemical availability/bioavailability of REEs in CFAs. Although sequential extraction does not provide direct insight into local coordination of Y or REE, it can assess their mobility under various environmental and geochemical conditions. Samples selected for sequential extraction were 5, 13, and 2S from the PRB, N. App, and PRB, respectively. Samples 5 and 13 contained <18% CaO, while 2S contained 28.7% CaO, and SCR technology was used for samples 13 and 2S (for more details, see Table 1). Direct phases associated with each sequential extraction step of CFAs are derived from Liu *et al.*,[31] based on XRD analysis of CFA residues after each step and dissolution of Y model compounds as affected by pH (PHREEQC calculations). Briefly, the pH of each sequential extraction step influences mineral dissolution, where the exchangeable fraction at pH 7 dissolves any adsorbed species, the acid-soluble fraction at pH 5 dissolves carbonates and oxides (as well as lime, periclase, and anhydrite), the reducible fraction at pH 2 with total dissolution of carbonates and partial dissolution of iron oxides (*i.e.*, hematite and magnetite), the oxidizable fraction at pH 2 with dissolution of organics, and the residual phase corresponds to the remaining aluminosilicates, phosphates, and incomplete dissolution of iron oxides.

The results for sequential extraction of all REEs are illustrated in Fig. 6. Unlike samples 5 and 2S, sample 13 had a majority of REEs (an average of 96%) in the residual fraction that is typically associated with aluminosilicate or zircon and incomplete dissolution of hematite (iron oxides), while samples 5 and 2S had a smaller portion of REEs in the residual fraction (an average of 87% and 79%). In addition to the residual fraction, the reducible fraction had the second highest REEs (averages of 11%, 3%, and 20% for samples 5, 13, and 2S, respectively), associated with partial dissolution of iron oxide phases and complete dissolution of carbonates. The complete dissolution of carbonates in the reducible fraction may explain the higher concentrations of REEs released in sample 2S, due to its higher CaO content, including anhydrite and lime in this sample. The acid-soluble fraction had the third highest REEs

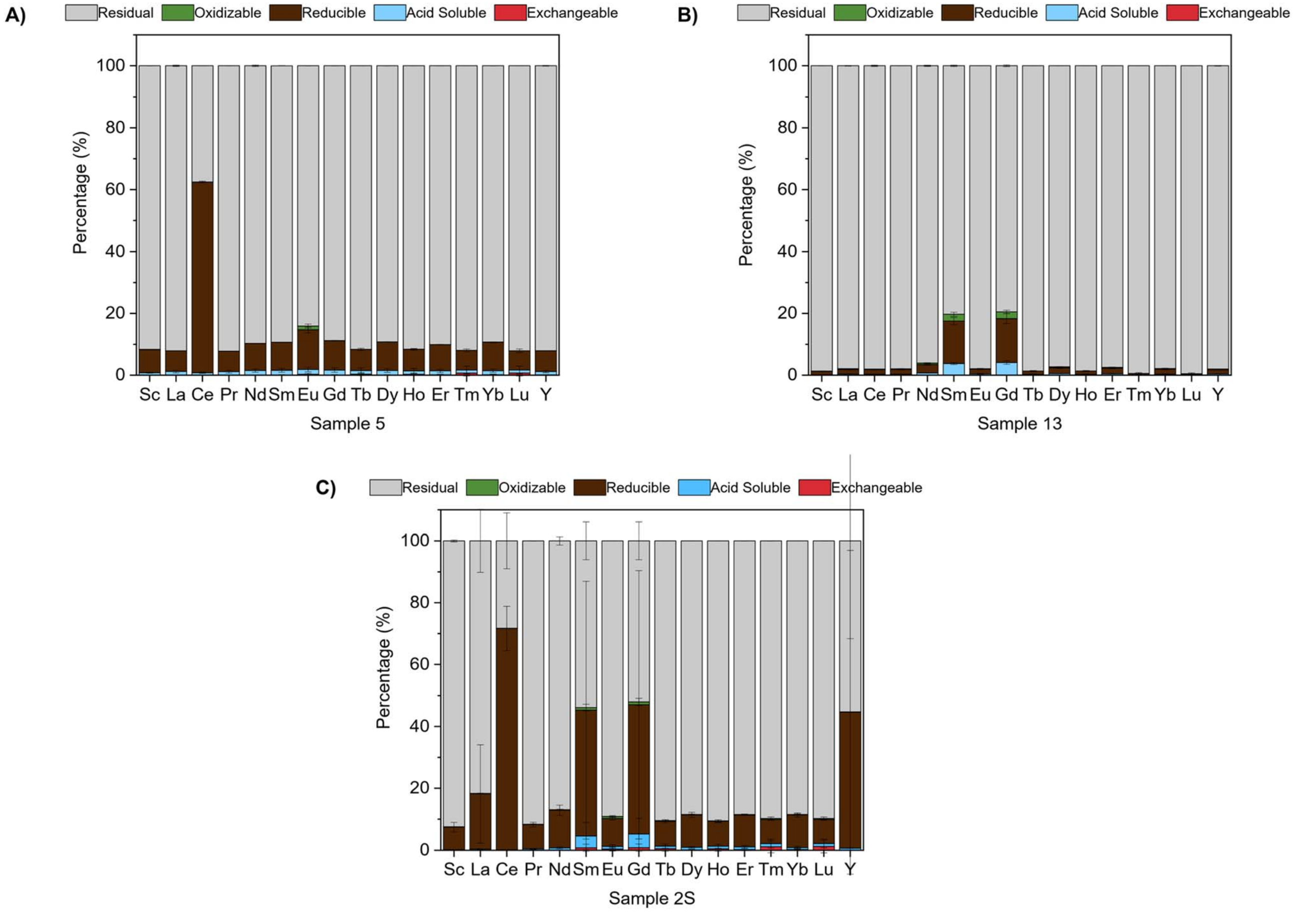

Fig. 6 Sequential extraction results for exchangeable (surface adsorbed species), acid soluble (carbonates), reducible (iron and manganese oxides), oxidizable (organic matter and sulfides), and residual (glass or aluminosilicates) fractions for REEs for (A) sample 5, (B) sample 13, and (C) sample 2S, shown as a percentage of the total in mg g^{-1} solid.

(an average of 1% for all samples), and the oxidizable fraction had the fourth highest REEs with an average of 0.1%, 0.4%, and 0.3% for samples 5, 13, and 2S, respectively. Lastly, the smallest portion of REEs was associated with the ion-exchangeable phase as 0%, 0%, and 0.4% for samples 5, 13, and 2S, respectively.

Overall, the sequential extraction results partially agree with the LCF results of bulk XANES. For example, sequential extraction results suggest that REEs are primarily associated with the glass, aluminosilicate, iron oxide, and phosphate fractions (79–96%), in agreement with the bulk XANES results that Y-glass, Y-phosphate (churchite), and Y-iron oxide (hematite) account for 72%, 25–41%, and 22–26% of Y speciation, respectively. Likewise, REEs associated with incomplete dissolution of carbonates (acid-soluble fraction), organics (oxidizable fraction), and adsorbed species (exchangeable fraction) are ≤1%, and these phases were not revealed by bulk XANES. This agrees with the fact that less thermally stable phases like carbonates and organics are not commonly found in CFA because they are prone to transformation into more stable phases (*e.g.*, oxides, phosphates, *etc.*) during high-temperature combustion.

On the other hand, while bulk XANES results revealed REE oxides (Y_2O_3) as a major fraction (28–78%) in all CFAs analyzed, sequential extraction indicates that only 1% of REEs are associated with oxides in the acid-soluble fraction. Such discrepancy can be attributed to several reasons. Discrepancies between XANES and sequential extraction may be due to their inherent limitations, and XANES does not provide direct information on physical distribution. REE-bearing particles may be trapped or encapsulated in acid-resistant silicate phases like glass and zircon that are formed by thermal transformation of mineral impurities during coal combustion.[31,59,67,68] Encapsulation of REE-bearing particles can significantly impede REE dissolution during sequential extraction, resulting in underestimation of more soluble REE-species (*e.g.*, oxides, carbonates, *etc.*) and overestimation of less soluble ones (*e.g.*, glass, zircon, *etc.*). The dominant presence of Y-glass (72.4%) in sample 9 could be such an example (Table 2), especially considering that quartz accounts for a significant fraction of its mineral phases (Figure S1). This also corroborates with results from sequential extraction that a majority of REEs (≥79%) may reside in the residual phase (associated with glass, iron oxide, or phosphate). Additionally, LCF is inherently incapable of distinguishing highly similar XANES spectra (*e.g.*, churchite *vs.* monazite;

tengerite *vs.* hematite; shown in Fig. S2) and may suggest different compositions of Y speciation without significantly compromising the fitting quality (*e.g.*, less than 5% change in the R-factor). These discrepancies may also be attributed to a limitation of sequential extraction, which is the partial dissolution of a given fraction, causing incomplete targeting between fractions. Although sequential extraction results are not in complete agreement with bulk XANES results in certain REE-species, both techniques complement each other and offer valuable insight into the chemical speciation and extractability of REEs in CFAs.

4. Conclusion

In this study, the chemical speciation of REEs in representative CFAs from 3 coal basins in the U.S. were systematically characterized by synchrotron XANES and XRF at both the macro- and micro-scales using Y as an REE probe. According to the LCF results of bulk XANES, Y is primarily present as 28–78% Y_2O_3, 29–41% Y-phosphate (churchite), and 22–26% hematite, except for 1 sample from PRB that contains 72% of Y as the glass phase. μ-XRF images revealed that REEs were found to colocalize together within particles. Importantly, CFAs were found to be highly heterogeneous in REE speciation at different spatial scales, which corroborates with previous studies. While μ-XANES analyses of individual Y-containing particles selected from μ-XRF images also indicate Y_2O_3, Y-phosphates, and Y-glass as the major REE-bearing phases, the predicted Y speciation of selected particles is notably different from the bulk XANES and even varies among different hot spots within the same particle. The heterogeneity of CFAs likely arises from the diverse REE host phases in the original coals, spatial variation in local bonding environments of REEs formed during coal combustion, and the inherent sampling bias of μ-XRF/μ-XANES. Sequential extraction suggests that REEs mainly exist in the residual fraction that is typically associated with silicate phases and iron oxides, which nevertheless can be overestimated due to inherent limitations of LCF. Lastly, the results from this study suggest that SCR may affect REE concentrations in CFAs, but further studies are needed to validate this. Owing to the representative nature of CFAs in this study, CFAs across the U.S. are crucial alternative REE sources with critical outlook coefficients greater than 0.9 and REE critical% greater than 36%.

Conflicts of interest

There are no conflicts to declare.

Data availability

Data associated with this study are presented in the supplementary information (SI) and are available upon request. Supplementary information is available. See DOI: https://doi.org/10.1039/d5em00857c.

Acknowledgements

This work was supported by the NSF grant # 2327660. This work was performed in part at the Georgia Tech Institute for Electronics and Nanotechnology, a member of the National Nanotechnology Coordinated Infrastructure (NNCI), which is supported by the National Science Foundation (ECCS-2025462). Portions of this work were conducted at the Stanford Synchrotron Radiation Lightsource (SSRL) at SLAC National Accelerator Laboratory and the Advanced Photon Source (APS) at Argonne National Laboratory, supported by the U.S. Department of Energy, Office of Science, Office of Basic Energy Sciences under contract No. DE-AC02-76SF00515 and DE-AC02-06CH11357.

References

1 B. S. Van Gosen, P. L. Verplanck, K. R. Long, J. Gambogi and R. R. Seal Ii, *The rare-earth elements: Vital to modern technologies and lifestyles*, Reston, VA, 2014, DOI: 10.3133/fs20143078, https://pubs.usgs.gov/publication/fs20143078.

2 C. L. T., DOD Looks to Establish 'Mine-to-Magnet, *Supply Chain for Rare Earth Materials*, 2024, https://www.defense.gov/News/News-Stories/Article/Article/3700059/dod-looks-to-establish-mine-to-magnet-supply-chain-for-rare-earth-materials/.

3 *Nomenclature of Inorganic Chemistry – IUPAC Recommendations 2005*, Chemistry International – Newsmagazine for IUPAC, 2005, vol. 27, 6, pp. 25–26, DOI: 10.1515/ci.2005.27.6.25, acccessed 2025-04-18.

4 V. Balaram, Rare earth elements: a review of applications, occurrence, exploration, analysis, recycling, and environmental impact, *Geosci. Front.*, 2019, **10**(4), 1285–1303, DOI: 10.1016/j.gsf.2018.12.005.

5 USGS, *Rare Earth Elements—Critical Resources for High Technology*, USGS, 2002, https://pubs.usgs.gov/fs/2002/fs087-02.

6 J. Dostal, Rare Earth Element Deposits of Alkaline Igneous Rocks, *Resources*, 2017, **6**(3), 34, DOI: 10.3390/resources6030034.

7 P. Chen, E. S. Ilton, Z. Wang, K. M. Rosso and X. Zhang, Global rare earth element resources: A concise review, *Appl. Geochem.*, 2024, **175**, 106158, DOI: 10.1016/j.apgeochem.2024.106158.

8 P. C. Keller and C. G. Anderson, The Production of Critical Material as By Products, *Aspects in Mining & Mineral Science*, 2018, **2**(2), 2–14, DOI: 10.31031/AMMS.2018.02.000532.

9 S. R. Golroudbary, I. Makarava, A. Kraslawski and E. Repo, Global environmental cost of using rare earth elements in green energy technologies, *Sci. Total Environ.*, 2022, **832**, 155022, DOI: 10.1016/j.scitotenv.2022.155022.

10 T. M. O'Brien and E. Alonso, A simplified rare earth element mining project cost estimator – a new tool for evaluating future mine supply, *Miner. Econ.*, 2025, **38**(2), 237–252, DOI: 10.1007/s13563-024-00467-6.

11 USGS, *United States Geological Survey Mineral Commodity Summaries*, 2021, https://pubs.usgs.gov/periodicals/mcs2025/mcs2025-rare-earths.pdf.

12 A. Boxleiter and W. C. Elliott, Rare-Earth Minerals in Kaolin Ore, Mine Tailings, and Sands – Central Georgia, Upper Coastal Plain, *Clays Clay Miner.*, 2023, **71**(3), 274–308, DOI: 10.1007/s42860-023-00235-7.

13 A. Boxleiter, Y. Wen, Y. Tang and W. C. Elliott, Rare-earth element (REE) remobilization and fractionation in bauxite zones from sedimentary kaolin deposits, western Georgia (USA), Upper Coastal Plain, *Chem. Geol.*, 2024, **660**, 122151, DOI: 10.1016/j.chemgeo.2024.122151.

14 A. Akcil, K. R. Swami, R. L. Gardas, E. Hazrati and S. Dembele, Overview on Hydrometallurgical Recovery of Rare-Earth Metals from Red Mud, *Minerals*, 2024, **14**, 587.

15 W. Li, Z. Li, N. Wang and H. Gu, Selective extraction of rare earth elements from red mud using oxalic and sulfuric acids, *J. Environ. Chem. Eng.*, 2022, **10**(6), 108650, DOI: 10.1016/j.jece.2022.108650.

16 Y. Wen, L. Hu, A. Boxleiter, D. Li and Y. Tang, Rare Earth Elements Recovery and Waste Management of Municipal Solid Waste Incineration Ash, *ACS Sustainable Resour. Manage.*, 2024, **1**(1), 17–27, DOI: 10.1021/acssusresmgt.3c00026.

17 E. Allegrini, A. Maresca, M. E. Olsson, M. S. Holtze, A. Boldrin and T. F. Astrup, Quantification of the resource recovery potential of municipal solid waste incineration bottom ashes, *Waste Manage.*, 2014, **34**(9), 1627–1636, DOI: 10.1016/j.wasman.2014.05.003.

18 Y. Wen, L. Hu, P. Liu, Q. Wang, E. Garcia, W. Yan and Y. Tang, Rare earth element (REE) speciation in municipal solid waste incineration ash, *Appl. Geochem.*, 2025, **178**, 106239, DOI: 10.1016/j.apgeochem.2024.106239.

19 J. C. Hower, J. G. Groppo, H. Hsu-Kim and R. K. Taggart, Distribution of rare earth elements in fly ash derived from the combustion of Illinois Basin coals, *Fuel*, 2021, **289**, 119990, DOI: 10.1016/j.fuel.2020.119990.

20 J. Yun, Q. Yang, C. Zhao, C. Chen and G. Liu, Atmospheric emissions of fine particle matter bound rare earth elements from industry, *Nat. Commun.*, 2024, **15**(1), 9338, DOI: 10.1038/s41467-024-53684-6.

21 B. Fu, J. C. Hower, W. Zhang, G. Luo, H. Hu and H. Yao, A review of rare earth elements and yttrium in coal ash: Content, modes of occurrences, combustion behavior, and extraction methods, *Prog. Energy Combust. Sci.*, 2022, **88**, 100954, DOI: 10.1016/j.pecs.2021.100954.

22 P. Liu, L. Yang, Q. Wang, B. Wan, Q. Ma, H. Chen and Y. Tang, Speciation transformation of rare earth elements (REEs) during heating and implications for REE behaviors during coal combustion, *Int. J. Coal Geol.*, 2020, **219**, 103371, DOI: 10.1016/j.coal.2019.103371.

23 R. K. Taggart, J. C. Hower, G. S. Dwyer and H. Hsu-Kim, Trends in the Rare Earth Element Content of U.S.-Based Coal Combustion Fly Ashes, *Environ. Sci. Technol.*, 2016, **50**(11), 5919–5926, DOI: 10.1021/acs.est.6b00085.

24 R. C. Reedy, B. R. Scanlon, D. A. Bagdonas, J. C. Hower, D. James, J. R. Kyle and K. Uhlman, Coal ash resources and potential for rare earth element production in the United States, *Int. J. Coal Sci. Technol.*, 2024, **11**(1), 74, DOI: 10.1007/s40789-024-00710-z.

25 A. C. A. Association, *Coal Combustion Products Production & Use Reports 2020*, 2020.

26 P. Liu, S. Zhao, N. Xie, L. Yang, Q. Wang, Y. Wen, H. Chen and Y. Tang, Green Approach for Rare Earth Element (REE) Recovery from Coal Fly Ash, *Environ. Sci. Technol.*, 2023, **57**(13), 5414–5423, DOI: 10.1021/acs.est.2c09273.

27 J. Hower, K. Henke, S. Dai, C. Ward, D. French, S. Liu and U. Graham, Generation and Nature of Coal Fly Ash and Bottom Ash, in *Coal Combustion Products (CCP's)*, ed. T. Robl, A. Oberlink, and R. Jones, Woodhead Publishing, 2017, pp. 21–65.

28 F. E. Huggins, C. L. Senior, P. Chu, K. Ladwig and G. P. Huffman, Selenium and Arsenic Speciation in Fly Ash from Full-Scale Coal-Burning Utility Plants, *Environ. Sci. Technol.*, 2007, **41**(9), 3284–3289, DOI: 10.1021/es062069y.

29 J. C. Hower, J. D. Robertson, G. A. Thomas, A. S. Wong, W. H. Schram, U. M. Graham, R. F. Rathbone and T. L. Robl, Characterization of fly ash from Kentucky power plants, *Fuel*, 1996, **75**(4), 403–411, DOI: 10.1016/0016-2361(95)00278-2.

30 G. P. Huffman, F. E. Huggins, N. Shah and J. Zhao, Speciation of arsenic and chromium in coal and combustion ash by XAFS spectroscopy, *Fuel Process. Technol.*, 1994, **39**(1), 47–62, DOI: 10.1016/0378-3820(94)90171-6.

31 P. Liu, R. Huang and Y. Tang, Comprehensive Understandings of Rare Earth Element (REE) Speciation in Coal Fly Ashes and Implication for REE Extractability, *Environ. Sci. Technol.*, 2019, **53**(9), 5369–5377, DOI: 10.1021/acs.est.9b00005.

32 R. K. Taggart, N. A. Rivera, C. Levard, J.-P. Ambrosi, D. Borschneck, J. C. Hower and H. Hsu-Kim, Differences in bulk and microscale yttrium speciation in coal combustion fly ash, *Environ. Sci.: Processes Impacts*, 2018, **20**(10), 1390–1403, DOI: 10.1039/c8em00264a.

33 M. Y. Stuckman, C. L. Lopano and E. J. Granite, Distribution and speciation of rare earth elements in coal combustion by-products *via* synchrotron microscopy and spectroscopy, *Int. J. Coal Geol.*, 2018, **195**, 125–138, DOI: 10.1016/j.coal.2018.06.001.

34 A. Kolker, C. Scott, J. C. Hower, J. A. Vazquez, C. L. Lopano and S. Dai, Distribution of rare earth elements in coal combustion fly ash, determined by SHRIMP-RG ion microprobe, *Int. J. Coal Geol.*, 2017, **184**, 1–10, DOI: 10.1016/j.coal.2017.10.002.

35 EPRI, *Survey of Coal-Fired Power Plants and Analysis of Selected Fly Ashes: A Task Toward Elucidating Arsenic and Selenium Speciation*, 2022, https://www.epri.com/research/products/000000003002025163.

36 J. Groppo, 1 – an introduction to the nature of coal, in *Coal Combustion Products (CCP's)*, ed. Robl, T., Oberlink, A. and Jones, R., Woodhead Publishing, 2017, pp. 3–20.

37 M. Mastalerz, A. Drobniak, J. C. Hower and J. M. K. O'Keefe, Chapter 3 – Spontaneous Combustion and Coal Petrology, in *Coal and Peat Fires: A Global Perspective*, ed. Stracher, G. B., Prakash, A. and Sokol, E. V., Elsevier, 2011, pp. 47–62.

38 P. Grammelis, N. Margaritis and E. Karampinis, 2 - Solid fuel types for energy generation: Coal and fossil carbon-derivative solid fuels, in *Fuel Flexible Energy Generation*, ed. Oakey, J., Woodhead Publishing, 2016, pp. 29–58.

39 ARC, *Subregions in Appalachia*, 2021, https://www.arc.gov/map/subregions-in-appalachia/.

40 E. Garcia, P. Liu, J. Sanchez, S. Lee, Q. Wang, Y. Wen, S. Shivaprakash, S. Burns and Y. Tang, A survey study on arsenic speciation in coal fly ash and insights into the role of coal combustion conditions, *Appl. Geochem.*, 2024, **170**, 106095, DOI: 10.1016/j.apgeochem.2024.106095.

41 B. Ravel and M. Newville, ATHENA, ARTEMIS, HEPHAESTUS: data analysis for X-ray absorption spectroscopy using IFEFFIT, *J. Synchrotron Radiat.*, 2005, **12**(4), 537–541, DOI: 10.1107/S0909049505012719.

42 S. Webb, The MicroAnalysis Toolkit: X-ray Fluorescence Image Processing Software, *AIP Conf. Proc.*, 2011, **1365**, 196–199, DOI: 10.1063/1.3625338.

43 S. M. Webb, SIXpack: a graphical user interface for XAS analysis using IFEFFIT, *Phys. Scr.*, 2005, **2005**(T115), 1011, DOI: 10.1238/Physica.Topical.115a01011.

44 R Core Team, *R: A Language and Environment for Statistical Computing*, R Foundation for Statistical Computing, Vienna, Austria, 2021, https://www.r-project.org/.

45 A. Tessier, P. C. G. Campbell and M. Bisson, Sequential Extraction Procedure for the Speciation of Particulate Trace Metals, *Anal. Chem.*, 1979, **51**(7), 844–851.

46 R. Winburn, D. Grier, G. McCarthy and R. Peterson, Rietveld Quantitative X-Ray Diffraction Analysis of NIST Fly Ash Standard Reference Materials, *Powder Diffr.*, 2000, **15**, 163–172, DOI: 10.1017/S0885715600011015.

47 P. Liu, Q. Wang, H. Jung and Y. Tang, Speciation, Distribution, and Mobility of Hazardous Trace Elements in Coal Fly Ash: Insights from Cr, Ni, and Cu, *Energy Fuels*, 2020, **34**(11), 14333–14343, DOI: 10.1021/acs.energyfuels.0c02164.

48 Energy.gov, *High Concentrations of Rare Earth Elements Found in American Coal Basins*, 2017, https://www.energy.gov/articles/high-concentrations-rare-earth-elements-found-american-coal-basins.

49 S. M. McLennan, Rare Earth Elements in Sedimentary Rocks: Influence of Provenance and Sedimentary Processes, *Rev. Mineral.*, 1989, **21**(1), 169–200.

50 V. V. Seredin and S. Dai, Coal deposits as potential alternative sources for lanthanides and yttrium, *Int. J. Coal Geol.*, 2012, **94**, 67–93, DOI: 10.1016/j.coal.2011.11.001.

51 D. A. Bagdonas, A. J. Enriquez, K. A. Coddington, D. C. Finnoff, J. F. McLaughlin, M. D. Bazilian, E. H. Phillips and T. L. McLing, Rare earth element resource evaluation of coal byproducts: A case study from the Powder River Basin, Wyoming, *Renewable Sustainable Energy Rev.*, 2022, **158**, 112148, DOI: 10.1016/j.rser.2022.112148.

52 R. K. Taggart, J. C. Hower, G. S. Dwyer and H. Hsu-Kim, Trends in the Rare Earth Element Content of U.S.-Based Coal Combustion Fly Ashes, *Environ. Sci. Technol.*, 2016, **50**(11), 5919–5926.

53 K. Pazand, Rare earth element geochemistry of coals from the Mazino Coal Mine, Tabas Coalfield, Iran, *Arabian J. Geosci.*, 2015, **8**(12), 10859–10869, DOI: 10.1007/s12517-015-1980-7.

54 S. Dai, D. Li, C.-L. Chou, L. Zhao, Y. Zhang, D. Ren, Y. Ma and Y. Sun, Mineralogy and geochemistry of boehmite-rich coals: New insights from the Haerwusu Surface Mine, Jungar Coalfield, Inner Mongolia, China, *Int. J. Coal Geol.*, 2008, **74**(3), 185–202, DOI: 10.1016/j.coal.2008.01.001.

55 P. P. Fedorov and N. V. Il'in, Yttrium carbonate thermolysis, *Russ. J. Inorg. Chem.*, 2012, **57**(2), 237–241, DOI: 10.1134/S0036023612020076.

56 I. C. Okeme, R. A. Crane, W. M. Nash, T. I. Ojonimi and T. B. Scott, Characterisation of rare earth elements and toxic heavy metals in coal and coal fly ash, *RSC Adv.*, 2022, **12**(30), 19284–19296, DOI: 10.1039/d2ra02788g.

57 E. Szatyłowicz and W. Walendziuk, Analysis of Polycyclic Aromatic Hydrocarbon Content in Ash from Solid Fuel Combustion in Low-Power Boilers, *Energies*, 2021, **14**, 6801.

58 E. Garcia, P. Liu, S. Bone, Y. Wen and Y. Tang, Systematic characterization of selenium speciation in coal fly ash, *Environ. Sci.: Processes Impacts*, 2024, **26**(12), 2240–2249, DOI: 10.1039/d4em00398e.

59 S. N. Montross, C. A. Verba, H. L. Chan and C. Lopano, Advanced characterization of rare earth element minerals in coal utilization byproducts using multimodal image analysis, *Int. J. Coal Geol.*, 2018, **195**, 362–372, DOI: 10.1016/j.coal.2018.06.018.

60 Y. Xia, Chapter eleven – correlation and association analyses in microbiome study integrating multiomics in health and disease, in *Progress in Molecular Biology and Translational Science*, ed. Sun, J., vol. 171, Academic Press, 2020, pp. 309–491.

61 H. B. Mann and D. R. Whitney, On a Test of Whether one of Two Random Variables is Stochastically Larger than the Other, *Ann. Math. Stat.*, 1947, **18**(1), 50–60, DOI: 10.1214/aoms/1177730491.

62 F. Wilcoxon, Individual Comparisons by Ranking Methods, *Biom. Bull.*, 1945, **1**(6), 80–83, DOI: 10.2307/3001968.

63 M. Hollander, D. A. Wolfe and E. Chicken, *Nonparametric Statistical Methods*, John Wiley & Sons, 2013.

64 E. L. Lehmann, *Nonparametrics: Statistical Methods Based on Ranks*, Prentice Hall, 1998.

65 W. W. Daniel, Kruskal–Wallis one-way analysis of variance by ranks, *Applied nonparametric statistics*, 1990, pp. 226–234.

66 W. H. Kruskal and W. A. Wallis, Use of Ranks in One-Criterion Variance Analysis, *J. Am. Stat. Assoc.*, 1952, **47**(260), 583–621, DOI: 10.1080/01621459.1952.10483441.

67 M. Hood, R. K. Taggart, R. Smith, H. Hsu-Kim, K. R. Henke, U. Graham, J. G. Groppo, J. M. Unrine and J. C. Hower, Rare Earth Element Distribution in Fly Ash Derived from the Fire Clay Coal, Kentucky, *Coal Combustion and Gasification Products*, 2017, **9**, 22–23, DOI: 10.4177/CCGP-D-17-00002.1.

68 J. C. Hower, B. Fu and S. Dai, Geochemical partitioning from pulverized coal to fly ash and bottom ash, *Fuel*, 2020, **279**, 118542, DOI: 10.1016/j.fuel.2020.118542.